Article

Dipole Moments Regulation of Biphosphonic Acid Molecules for Self-assembled Monolayers Boosts the Efficiency of Organic Solar Cells Exceeding 19.7%

Hang Liu,[⊥] Yufei Xin,[⊥] Zhaochen Suo, Liu Yang, Yu Zou, Xiangjian Cao, Ziyang Hu, Bin Kan, Xiangjian Wan, Yongsheng Liu,* and Yongsheng Chen*

ACCESS | 📊 Metrics & More | 📖 Article Recommendations | 🆂ᴵ Supporting Information

ABSTRACT: PEDOT:PSS has been widely used as a hole extraction layer (HEL) in organic solar cells (OSCs). However, their acidic nature can potentially corrode the indium tin oxide (ITO) electrode over time, leading to adverse effects on the longevity of the OSCs. Herein, we have developed a class of biphosphonic acid molecules with tunable dipole moments for self-assembled monolayers (SAMs), namely, 3-BPIC(i), 3-BPIC, and 3-BPIC-F, which exhibit an increasing dipole moment in sequence. Compared to centrosymmetric 3-BPIC(i), the axisymmetric 3-BPIC and 3-BPIC-F exhibit higher adsorption energies (E_{ads}) with ITO, shorter interface spacing, more uniform coverage on ITO surface, and better interfacial compatibility with the active layer. Thanks to the incorporation of fluorine atoms, 3-BPIC-F exhibits a deeper highest occupied molecular orbital (HOMO) energy level and a larger dipole moment compared to 3-BPIC, resulting in an enlarged work function (WF) for the ITO/3-BPIC-F substrate. These advantages of 3-BPIC-F could not only improve hole extraction within the device but also lower the interfacial impedance and reduce nonradiative recombination at the interface. As a result, the OSCs using SAM based on 3-BPIC-F obtained a record high efficiency of 19.71%, which is higher than that achieved from the cells based on 3-BPIC(i) (13.54%) and 3-BPIC (19.34%). Importantly, 3-BPIC-F-based OSCs exhibit significantly enhanced stability compared to that utilizing PEDOT:PSS as HEL. Our work offers guidance for the future design of functional molecules for SAMs to realize even higher performance in organic solar cells.
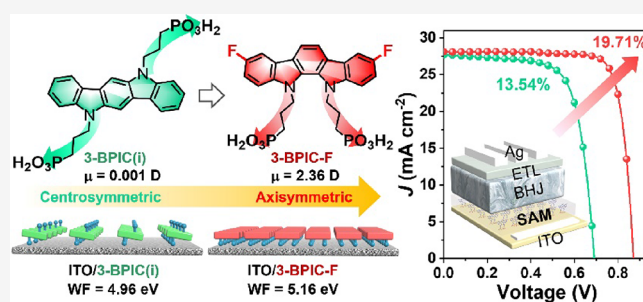
1. INTRODUCTION

Organic solar cells (OSCs) are regarded as one of the promising next-generation photovoltaic technologies thanks to their low cost, light weight, and mechanical flexibility.[1−9] Recently, the certified power conversion efficiency (PCE) of single junction OSCs has reached 19.4% benefiting from the rapid development of polymer donors and near-infrared (NIR) nonfullerene acceptors (NFAs).[10−21] Notably, charge transport layers (CTLs) also play a key role in carrier extraction and transport, which is essential for enhancing the performance of OSCs.[22,23] So far, the hole extraction layers (HELs) are dominated by PEDOT:PSS in regular OSCs.[5,22,24] However, the acidic nature of PEDOT:PSS due to the presence of the sulfonic acid groups in the PSS component can corrode the indium tin oxide (ITO) electrode over time, which is detrimental to the long-term stability of the OSCs.[25,26] Therefore, it is critically important to develop new alternatives to replace PEDOT:PSS in order to improve the long-term stability and efficiency of the OSCs.

Recently, self-assembled monolayers (SAMs) have been widely used in perovskite solar cells and have made great progress thanks to its simple molecular structure, low synthesis cost, low dosage, and adjustable energy levels.[27−33] Recently, SAMs have also received attention in the field of OSCs as a HEL alternative to PEDOT:PSS. In 2020, Anthopoulos and co-workers first used 2PACz as HEL in conventional OSCs, showing improved photovoltaic performance compared to that using PEDOT:PSS.[34] Then in 2022, they further developed the 3,6-dichlorosubstituted derivative (3,6-Cl-2PACz), which achieved a high PCE of 18.9% in PM6:PM7-Si:BTP-ec9-based OSCs.[35] Recently, Wang et al. successfully synthesized the more stable isomer 4,5-Cl-2PACz, which delivered an efficiency of 19.05% in a ternary device of PM6:BTP-ec9:L8-BO-F.[26] Except the widely used monophosphoric 2PACz and its derivatives, the increase in the number of phosphonic acid anchoring groups of molecules for SAMs is an alternative
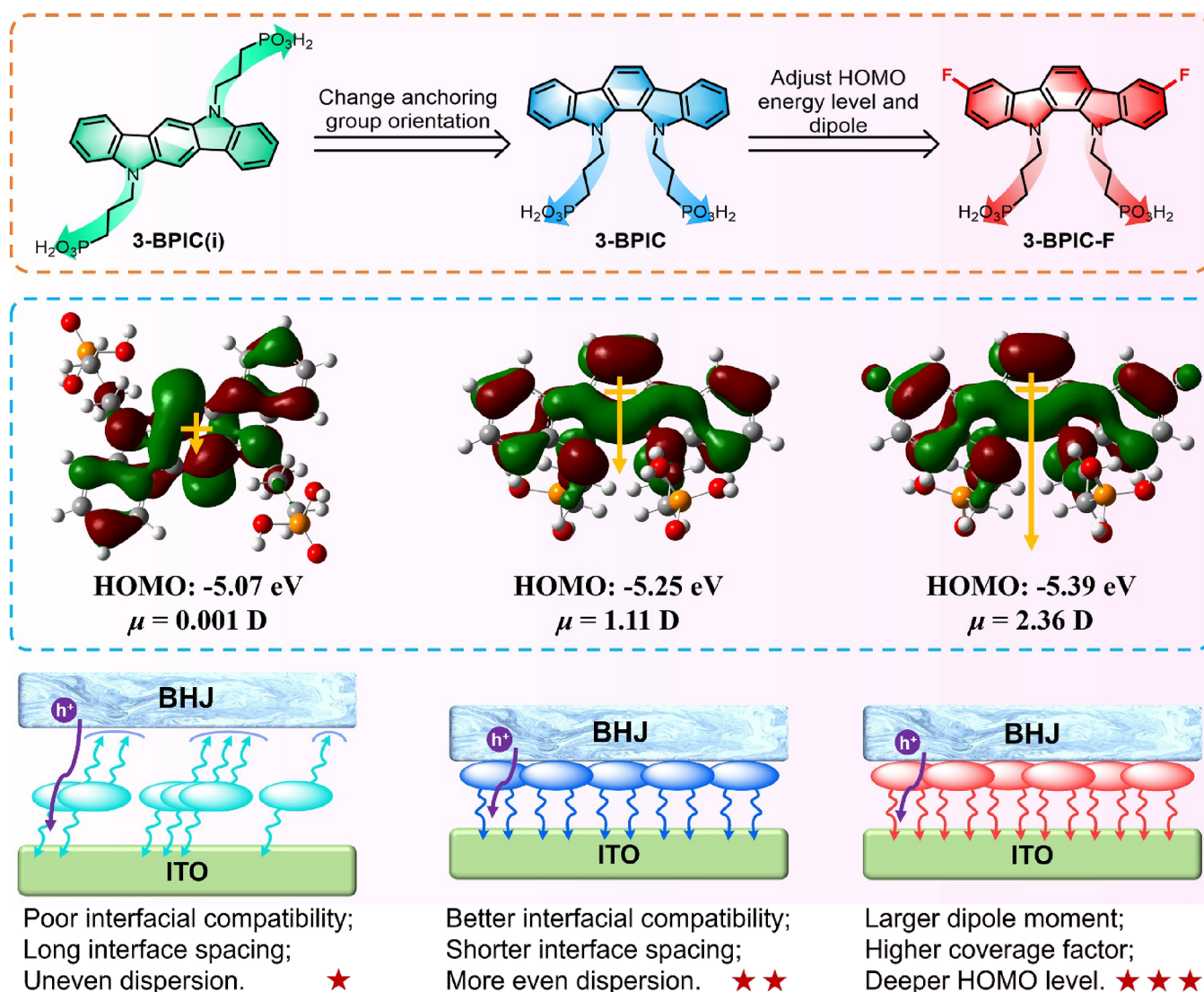
Figure 1. Molecular design, calculated HOMO orbital distributions, dipole moments, and HOMO energy levels of 3-BPIC(i), 3-BPIC, and 3-BPIC-F SAMs.

choice. These molecules could be adsorbed more firmly on the surface of ITO and improve the molecular coverage of SAM.[36] However, SAMs based on organic molecules featuring multiple phosphonic acid groups have rarely been reported in OSCs.

In this work, we have successfully developed a series of novel SAMs based on indolo[3,2-*b*]carbazole and indolo[2,3-*a*]-carbazole conjugate cores, which are named (indolo[3,2-*b*]carbazole-5,11-diylbis(propane-3,1-diyl))bis(phosphonic acid) (3-BPIC(i)), (indolo[2,3-*a*]carbazole-11,12-diylbis-(propane-3,1-diyl))bis(phosphonic acid) (3-BPIC), and ((3,8-difluoroindolo[2,3-*a*]carbazole-11,12-diyl)bis(propane-3,1-diyl))bis(phosphonic acid) (3-BPIC-F) (Figure 1), respectively. These molecules exhibit an increasing dipole moment in sequence. Compared to centrosymmetric 3-BPIC(i), the axisymmetric 3-BPIC and 3-BPIC-F show enhanced adsorption capabilities on the ITO surface, leading to improved surface coverage, more even distribution on the ITO surface, and shortened interface spacing between photoactive layer and ITO substrate. With the incorporation of fluorine atoms, 3-BPIC-F exhibits an enlarged dipole moment and a deeper highest occupied molecular orbital (HOMO) energy level, resulting in an enlarged work function

(WF) for ITO/3-BPIC-F substrate, thereby facilitating efficient hole extraction. Moreover, the fused aromatic structure on the opposite side of the phosphonic acid groups enhances their interfacial compatibilities with the photoactive layer. As a result, the 3-BPIC-F-based device achieved a champion PCE of 19.71%, much higher than that of devices based on 3-BPIC(i) (13.54%) and 3-BPIC (PCE = 19.34%). Moreover, the large-area (1.0 cm^2) device based on 3-BPIC-F achieved a high PCE of 17.25%.

2. RESULTS AND DISCUSSION

The synthetic routes of 3-BPIC(i), 3-BPIC, and 3-BPIC-F are illustrated in Supporting Information (Schemes S1−S3). The optical band gaps (E_g) of these molecules in films were estimated to be 2.92 eV for BPIC(i), 3.29 eV for 3-BPIC, and 3.12 eV for 3-BPIC-F, based on the ultraviolet−visible (UV−vis) absorption spectra (Figure S1a). Note that these SAM-coated ITO substrates exhibit light transmittance similar to that of bare ITO (Figure S1b), resulting in much enhanced light utilization compared to the ITO/PEDOT:PSS anode. The HOMO energy levels of 3-BPIC(i), 3-BPIC, and 3-BPIC-F were measured to be −4.98, −5.30, and −5.33 eV,
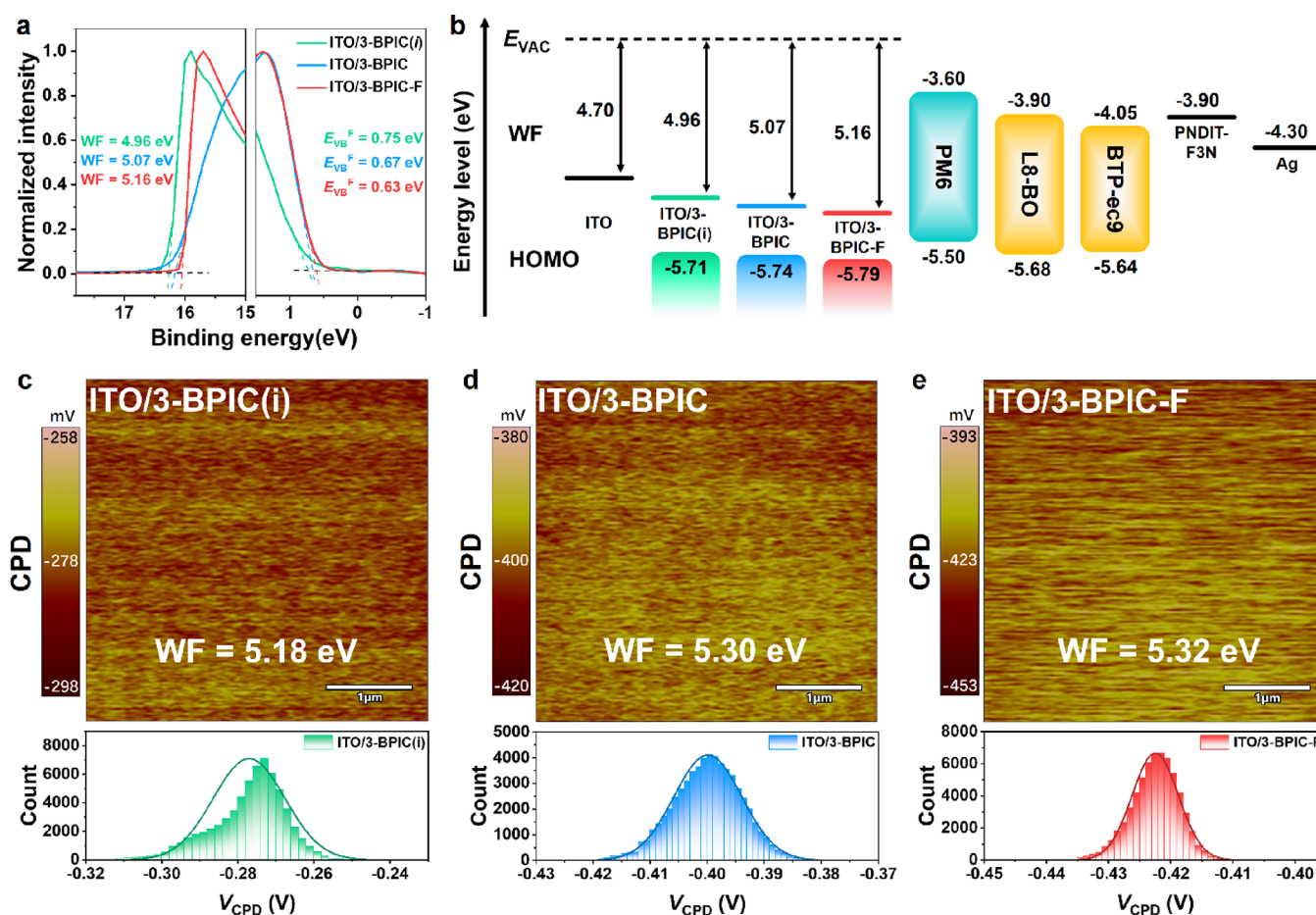
Figure 2. (a) UPS spectra of SAMs-modified ITO; (b) schematic diagram of energy level arrangement; (c−e) Kelvin probe atomic force microscopy (KPFM) images and surface contact potential distributions of ITO/3-BPIC(i), ITO/3-BPIC, and ITO/3-BPIC-F films.

respectively, by employing cyclic voltammetry (CV) measurement (Figure S2). The corresponding lowest unoccupied molecular orbital (LUMO) energy levels were calculated to be −2.06, −2.01, and −2.21 eV, respectively. These values agree well with the results of density functional theory (DFT) calculation (B3LYP/6-31G(d,p)) (Figure 1, Figure S3, and Table S1). The ultraviolet photoelectron spectrometry (UPS) analysis of ITO/SAM substrates reveals that the HOMO energy levels of ITO/3-BPIC(i), ITO/3-BPIC, and ITO/3-BPIC-F are −5.71, −5.74, and −5.79 eV (Figure 2a,b and Table S2), respectively, showing the same trend as observed from CV measurements and DFT calculations. The deeper HOMO energy level of ITO/3-BPIC-F is beneficial for the hole extraction, favoring an increase in the open circuit voltage (V_{OC}) of the device.[28,29]

After the ITO surface is modified with these SAMs, the WF of ITO will change to different degrees. The DFT results shows that the WF values of ITO, ITO/3-BPIC(i), ITO/3-BPIC, and ITO/3-BPIC-F were located at 4.86, 5.65, 5.69, and 5.72 eV, respectively (Figure S4 and Table S2). The calculated results are well in agreement with the UPS results (Figure 2a, Figure S5, and Table S2), which show a sequential increase in WF from 4.71 eV for ITO to 4.96 eV for ITO/3-BPIC(i), 5.07 eV for ITO/3-BPIC and 5.16 eV for ITO/3-BPIC-F. The largest dipole moment of 3-BPIC-F as calculated from DFT calculation may contribute to the enlarged WF for ITO/3-BPIC-F (Figure 1), thereby enhancing its compatibility with the HOMO energy level of the polymer donor PM6 in the

photoactive layer.[37,38] This will facilitate the hole extraction at the interface by minimizing the energy offset to achieve an higher fill factor (FF) and a larger open-circuit voltage (V_{OC}) of the corresponding OSCs.[37,39]

Kelvin probe atomic force microscopy (KPFM) was further performed to measure the surface potential of these substrates (Figure 2c−e and Figure S6). The WF was calculated to be 5.04 eV for ITO, 5.18 eV for ITO/3-BPIC(i), 5.30 eV for ITO/3-BPIC, and 5.32 eV for ITO/3-BPIC-F without corrections (Table S2). This exhibits a trend similar to that of the WF values obtained from UPS spectra. It is worth noting that ITO/3-BPIC and ITO/3-BPIC-F exhibit narrower surface contact potential distribution (CPD) compared to ITO/3-BPIC(i) (Figure 2c−e), indicating a more uniform coverage of 3-BPIC and 3-BPIC-F on the ITO surface.

The phosphonic acid anchoring group orientation of the SAM molecule will affect its adsorption properties on the ITO surface and its interfacial compatibility with the bulk-heterojunction (BHJ) active layer. The chemical adsorption simulation of these SAM molecules (Figure 3a−c) using DFT calculation reveal that the two phosphonic acid groups of axisymmetric 3-BPIC and 3-BPIC-F are oriented on the same sides, whereas those phosphonic acid groups of centrosymmetric 3-BPIC(i) are oriented on the opposite sides when adsorbed on ITO. The adsorption energies (E_{ads}) of 3-BPIC and 3-BPIC-F on ITO were calculated to be −2.17 and −2.40 eV, respectively, apparently higher than that of 3-BPIC(i) on ITO (−1.43 eV). Furthermore, these adsorption simulation
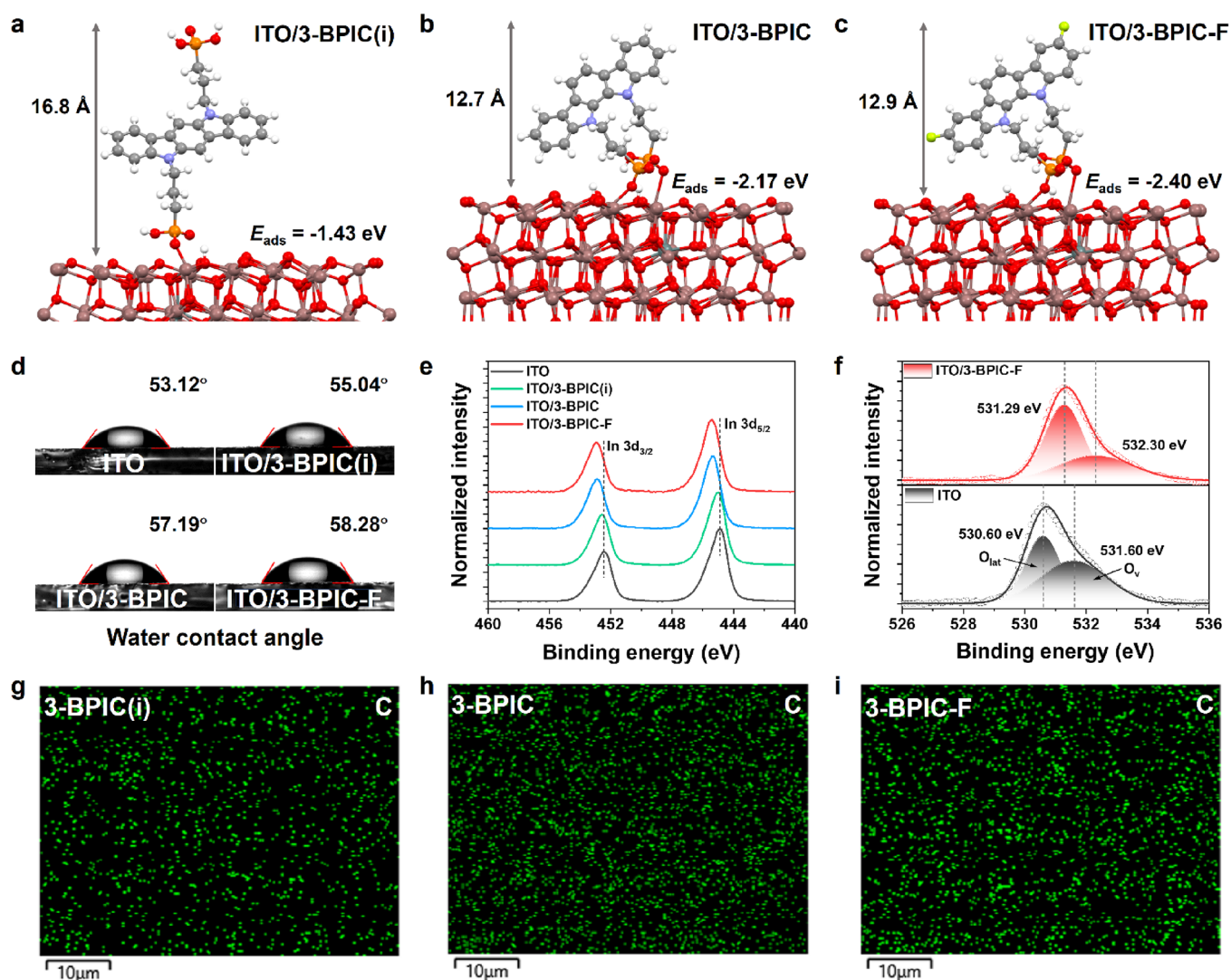
Figure 3. (a−c) Chemical adsorption models of 3-BPIC(i), 3-BPIC, and 3-BPIC-F on the ITO (111) surface; (d) water contact angles images of bare ITO and ITO/SAMs films; (e) In 3d core level X-ray photoelectron spectroscopy (XPS) spectra of the bare ITO and ITO/SAMs films; (f) O 1s core level XPS spectra of bare ITO and ITO/3-BPIC-F films; (g−i) elemental mapping of C for 3-BPIC(i), 3-BPIC, and 3-BPIC-F-modified ITO.

results display that 3-BPIC and 3-BPIC-F have interface spacings of 12.7 and 12.9 Å, respectively, much shorter than that of 3-BPIC(i) (16.8 Å). The improvement in E_{ads} and the reduction in interface spacing of 3-BPIC-F SAM layer will facilitate the coverage of 3-BPIC-F on the ITO surface and improve the hole extraction from the BHJ active layer. In addition, the conjugated units in the SAMs based on 3-BPIC and 3-BPIC-F are expected to exhibit better interface compatibility with the upper BHJ layer compared to ITO/3-BPIC(i), which demonstrates limited compatibility between the phosphonic acid groups and the BHJ layer as discussed below.

To prove the above chemical adsorption model, we performed contact angle (CA) measurements for water and diiodomethane (DIM). As shown in Figure 3d, the water contact angle of ITO/3-BPIC(i) was measured to be 55.04°, which is smaller than that of ITO/3-BPIC (57.19°) and ITO/3-BPIC-F (58.28°). The DIM contact angle in Figure S7 shows that the ITO/3-BPIC-F substrate exhibits a smaller value of 26.89° compared to that of ITO/3-BPIC(i) (39.07°) and ITO/3-BPIC (29.86°). These results indicate that 3-BPIC and

3-BPIC-F SAMs have better interface compatibility with organic photoactive layer, in good agreement with the chemical adsorption model discussed above.

The adsorption properties of these SAMs were further investigated by X-ray photoelectron spectroscopy (XPS) measurements. As shown in Figure 3d and Table S3, the In $3d_{3/2}$ and In $3d_{5/2}$ peaks for bare ITO were located at 452.45 and 444.89 eV, respectively. For SAMs-covered ITO, these peaks were shifted to 452.58 and 445.02 eV for 3-BPIC(i), 452.90 and 445.35 eV for 3-BPIC, and 452.95 and 445.43 eV for 3-BPIC-F, respectively. The similar trend was also observed for the Sn 3d peaks (Figure S8 and Table S3). Similarly, the O 1s peaks for bare ITO, ITO/3-BPIC(i), ITO/3-BPIC, and ITO/3-BPIC-F were located at 530.60 530.80, 531.14, and 531.29 eV, respectively, according to the lattice oxygen (O_{lat}) present on the surface of the ITO film (Figure 3e and Figure S9). The gradually increased shifts of the In 3d, O 1s, and Sn 3d orbitals from the ITO/3-BPIC(i), ITO/3-BPIC, and ITO/3-BPIC-F, compared to bare ITO, suggest an enlarged interaction between the SAMs and ITO, consistent with the increased E_{ads} calculated above.[29,40] In addition, the ratio of
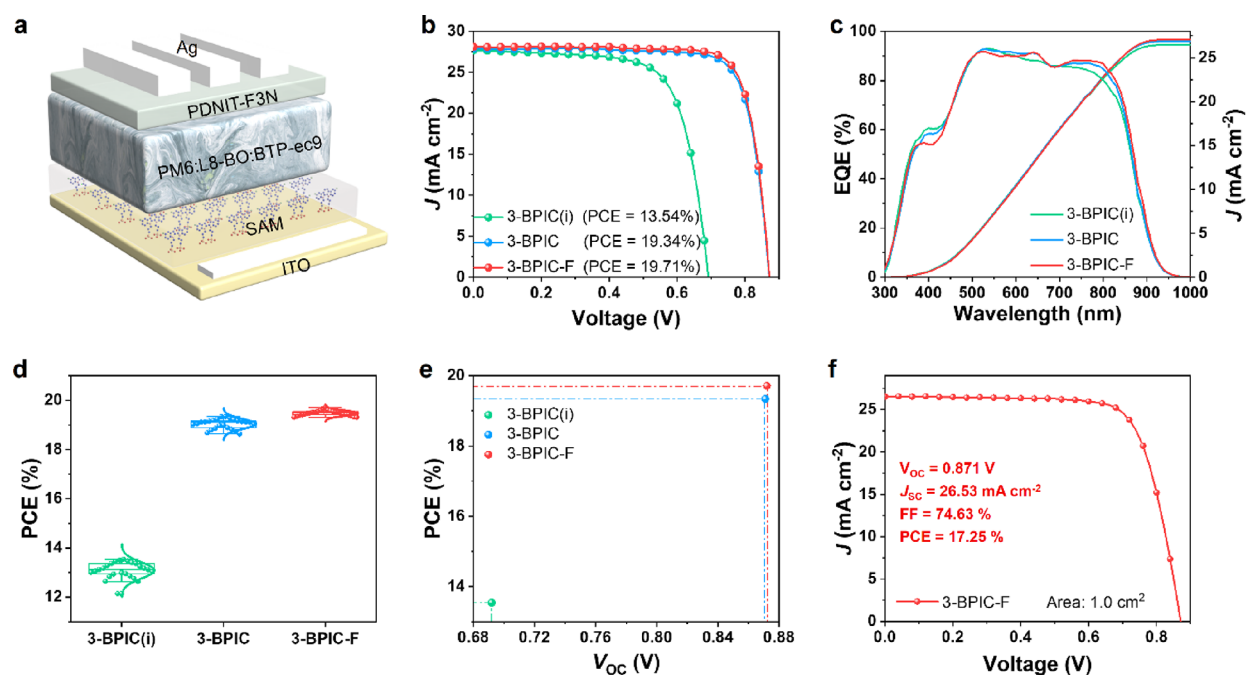
Figure 4. (a) Device architecture of the conventional OSCs based on SAMs; (b) $J-V$ characteristics curves of the PM6:L8-BO:BTP-ec9 device based on three SAMs; (c) EQE spectra and integrated photocurrent density of the corresponding devices; (d) statistical PCE data of the corresponding devices; (e) PCE and V_{OC} values of the corresponding devices. (f) $J-V$ curve of the large-area OSC device (area: 1.0 cm^2) based on 3-BPIC-F.

Table 1. Optimized Photovoltaic Parameters for Devices Based on Different SAMs and PEDOT:PSS

BHJ	HEL	V_{OC} [V]	J_{SC} [mA cm^{-2}]	J_{SC}[a] [mA cm^{-2}]	FF [%]	PCE [%]
PM6: L8-BO: BTP-ec9	3-BPIC(i)	0.692 (0.686 ± 0.019)	27.68 (26.84 ± 0.63)	26.48	70.71 (71.21 ± 0.77)	13.54 (13.12 ± 0.33)
	3-BPIC	0.871 (0.866 ± 0.004)	27.89 (27.91 ± 0.25)	26.88	79.61 (78.65 ± 0.67)	19.34 (19.03 ± 0.20)
	3-BPIC-F	0.872 (0.872 ± 0.004)	28.12 (27.99 ± 0.12)	27.06	80.43 (79.83 ± 0.38)	19.71 (19.48 ± 0.11)
	PEDOT:PSS	0.860 (0.860 ± 0.002)	27.69 (27.28 ± 0.36)	26.52	78.59 (78.21 ± 0.73)	18.74 (18.34 ± 0.22)

[a]Calculated from EQE data.

vacancy oxygen (O_v) to O_{lat} was decreased from 0.95 for ITO to 0.93 for ITO/3-BPIC(i), 0.66 for ITO/3-BPIC, and 0.62 for ITO/3-BPIC-F (Figure 3f, Figures S9 and S10, and Table S3), indicating that oxygen vacancy defects were effectively passivated by phosphonic acid groups. Note that the high levels of coverage for 3-BPIC-F SAMs on ITO as discussed below should play a key role in the largely reduced oxygen vacancy defects. This will be conducive to the reduction of trap-assisted nonradiative recombination in OSCs.[40]

According to the peak areas of C 1s and In 3d observed in XPS surveys (Figure S11),[28] the coverage factor for 3-BPIC-F-modified ITO was calculated to be 1.26×10^{-2}, exceeding those of 1.10×10^{-2} for 3-BPIC-modified ITO and 6.01×10^{-3} for 3-BPIC(i)-modified ITO (Table S4). Moreover, the atomic concentration ratios of 3-BPIC-F modified ITO obtained from the XPS surveys (Table S5) also show a higher P/In ratio of 0.45 compared to 0.35 and 0.42 for 3-BPIC(i)- and 3-BPIC-modified ITO, respectively, suggesting a better coverage of 3-BPIC-F on the ITO substrate. The energy-dispersive X-ray spectroscopy (EDS) (Figure 3g-i and Figure S12) shows the element mass fraction (wt) of C and P, which could be used to evaluate the coverage of SAMs on the ITO surface. Because these molecules contain the same number of carbon atoms and phosphorus atoms, the molecular concentration of these SAMs can be described by semiquantitative

analysis of the ratio of wt_C/wt_{In} and wt_P/wt_{In}. As shown in Table S6, the wt_C/wt_{In} and wt_P/wt_{In} for ITO/3-BPIC(i), ITO/3-BPIC, and ITO/3-BPIC-F were calculated to be 0.040 and 0.018, 0.045 and 0.020, and 0.051 and 0.021, respectively. The larger ratio of wt_C/wt_{In} and wt_P/wt_{In} indicates that 3-BPIC-F has a higher coverage factor, consistent with the coverage factor results obtained from XPS surveys above. This could be attributed to the same side-oriented phosphonic acid groups and higher E_{ads} of 3-BPIC-F.

According to the C−C stretching vibration characteristic absorption peak of the indolocarbazole core characterized by infrared (IR) absorption spectra (Figure S13), we performed atomic force microscopy-infrared spectroscopy (AFM-IR) measurements to further assess the coverage of these SAMs on the ITO surface. The AFM-IR images (Figure S14) demonstrated a similar trend to EDS results according to the enhanced IR response from 3-BPIC(i) to 3-BPIC-F.[41] Moreover, the AFM-IR images reveal that the 3-BPIC and 3-BPIC-F SAMs exhibited more uniform dispersions on ITO substrates, in agreement with the KPFM analysis above. The more uniform dispersion of 3-BPIC-F was further confirmed by a smaller root-mean-square (RMS) roughness of ITO/3-BPIC-F (1.98 nm) than that of ITO/3-BPIC(i) (2.81 nm) and ITO/3-BPIC (2.07 nm) (Figure S15), which will enhance the interface contact between BHJ active layer and substrate.[42]
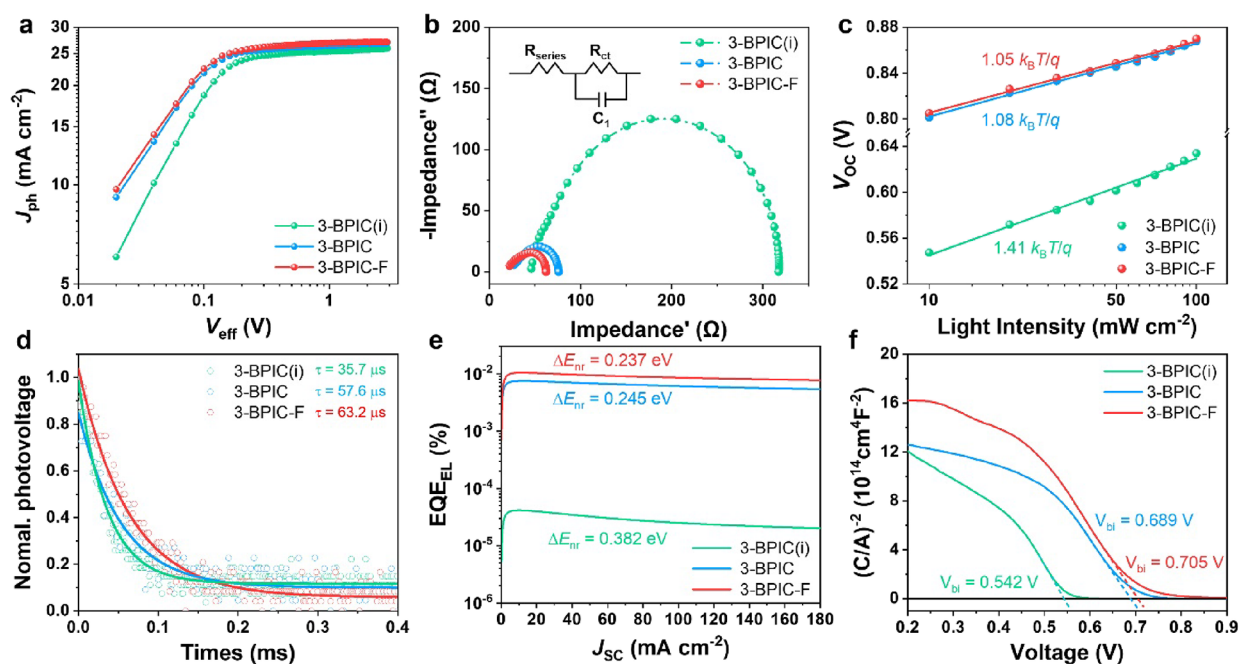
Figure 5. (a) Photocurrent density versus effective voltage ($J_{ph}-V_{eff}$) characteristics for the corresponding devices; (b) Nyquist plots of the corresponding devices (inset: equivalent-circuit model employed for fitting of EIS data); (c) V_{OC} versus light intensity for OSCs with different SAMs; (d) transient photovoltage measurements of the corresponding devices analyzed by a single-exponential decline model; (e) EQE_{EL} profiles of the corresponding devices; (f) Mott−Schottky plots of devices based on different SAMs.

To estimate the photovoltaic performance of these biphosphonic acid molecules for SAMs in OSCs, we fabricated the devices with a conventional structure of ITO/SAM/BHJ/PNDIT-F3N/Ag (Figure 4a) and PM6:L8-BO:BTP-ec9 (chemical structure in Figure S16) was selected as the BHJ components.[21] The preparation process of SAM-modified ITO is illustrated in Figure S17, and the SAM concentration optimization details are shown in Figure S18 and Table S7. The devices based on PEDOT:PSS were also fabricated for comparison. The current density−voltage ($J-V$) curves of OSCs in Figure 4b show that the device using SAM based on centrosymmetric 3-BPIC(i) exhibits a V_{OC} of 0.692 V, a short-circuit current density (J_{SC}) of 27.68 mA cm^{-2}, and a fill factor (FF) of 70.71%, achieving a PCE of 13.54% (Table 1). The OSCs based on axisymmetric 3-BPIC SAM show a higher PCE of 19.34% with an improvement in J_{SC} (27.89 mA cm^{-2}), V_{OC} (0.871 V), and FF (79.61%). In particular, the optimized OSCs based on axisymmetric 3-BPIC-F demonstrated further improvement with an enlarged J_{SC} of 28.12 mA cm^{-2}, notable FF of 80.43%, and V_{OC} of 0.872 V, yielding a champion PCE of 19.71%, much higher than that of the PEDOT:PSS-based device (PCE = 18.74%, Figure S20 and Table 1). Notably, the PCE of 19.71% is the highest value reported to date for OSCs based on SAMs as the HEL (Table S10).[26,33−35,43−47] The distributions of photovoltaic parameters of OSCs with different HELs are displayed in Figure 4d and Figures S19 and S21. Standard deviations and statistics of PCEs from OSCs show that the devices based on 3-BPIC-F exhibit an average PCE of 19.48%, surpassing those of 3-BPIC(i) (PCE$_{avg}$ = 13.12%), 3-BPIC (PCE$_{avg}$ = 19.03%), and PEDOT:PSS (PCE$_{avg}$ = 18.34%). The improvement in PCE from devices based on 3-BPIC(i) to those based on 3-BPIC and 3-BPIC-F was mainly due to an increase in V_{OC} (Figure 4e), which could be attributed to the enlarged WF of ITO/3-BPIC-F and the increased built-in voltage (V_{bi}) of the device as discussed

below. Additionally, the integrated J_{SC} of OSCs based on 3-BPIC(i), 3-BPIC, and 3-BPIC-F calculated from external quantum efficiency (EQE) curves (Figure 4c) were 26.48, 26.88, and 27.06 mA cm^{-2}, respectively, in good agreement with the $J-V$ results with an error within 4%. Thanks to the exceptional photophysical properties and superior film quality of 3-BPIC-F SAM, the large-area (1.0 cm^2) device delivered a champion efficiency of 17.25%, accompanied by a J_{SC} of 26.53 mA cm^{-2}, a V_{OC} of 0.871 V, and an FF of 74.63% (Figure 4f and Table S8). To verify the superiority of 3-BPIC-F HEL, we have employed various BHJ systems in the OSCs, and all the devices exhibited improved efficiency compared to PE-DOT:PSS-based devices (Figure S22 and Table S9).

Besides the improvement of PCEs, we also accessed the stability of unencapsulated OSCs. As shown in Figure S23, the 3-BPIC-F-based OSC exhibits better storage stability than the OSC based on PEDOT:PSS after storing for nearly 800 h in a N$_2$ glovebox at room temperature. Under the condition of 65 °C heating in a N$_2$ glovebox, the unencapsulated device based on 3-BPIC-F maintained an initial PCE of over 80% after aging for 700 h, while the PCE of unencapsulated OSC based on PEDOT:PSS decayed to less than 80% of its initial value after 300 h (Figure S24).

To study the charge transport properties of these SAM molecules, we carried out electrical conductivity measurements using devices with the structure of ITO/SAMs/Ag. As shown in Figure S25, the electrical conductivities of 3-BPIC(i), 3-BPIC, and 3-BPIC-F were measured to be 4.07×10^{-5}, 4.42×10^{-5}, and 4.77×10^{-5} S m^{-1}, respectively. The higher conductivity of 3-BPIC-F among these molecules could be attributed to its axisymmetric structure and higher coverage factor, which contributed to improved device performance.

The exciton dissociation and charge collection properties of the OSCs with these HELs were then evaluated. Figure 5a shows the curves of the photocurrent density (J_{Ph}) with respect

to the effective bias voltage (V_{eff}). The charge dissociation probabilities (P(E,T)) of 3-BPIC(i), 3-BPIC, and 3-BPIC-F-based devices were 97.8%, 98.2%, and 98.8% (for the short-circuit condition), respectively, and 88.0%, 89.3%, and 91.4% (for the maximal power output condition), respectively. The enhanced P(E,T) of 3-BPIC-F-based device suggests that less driving force is needed to extract the carriers from the BHJ.[48] The $J-V$ characteristics of SAMs-based OSCs in the dark state are displayed in Figure S26. The improved current density at a positive bias and reduced leakage current under a reverse bias voltage of 3-BPIC-F-based device indicates a decreased series resistance (R_{series}) and a suppressed electron injection at anode interface, respectively.[49,50]

As shown in Figure 5b, the Nyquist plot of the electrochemical impedance spectroscopy (EIS) spectra was measured for OSCs based on different SAMs. According to the equivalent-circuit model, the series resistance and charge-transport resistance (R_{ct}) of devices based on 3-BPIC(i), 3-BPIC, and 3-BPIC-F are as follows: 46.9 and 317.7 Ω, 27.0 and 75.9 Ω, and 22.2 and 62.1 Ω, respectively. The reduction in both R_{series} and R_{CT} of 3-BPIC-F-based devices could be attributed to the shortened interface spacing and improved interface compatibility, which are beneficial for carrier transport and for suppressing charge recombination, thereby improving the FF of the devices.[51]

To study the carrier recombination kinetics in OSCs based on different SAMs, the light-intensity-dependent $J-V$ characteristics were evaluated. The relationship between V_{OC} and light intensity (I) follows the formula $V_{OC} \propto nk_BT\ln(I)/q$, where k_B, T, q, and n are the Boltzmann constant, Kelvin temperature, elementary charge, and ideality factor, respectively.[52] The n values of 3-BPIC(i), 3-BPIC, and 3-BPIC-F-based OSCs are 1.41, 1.08, and 1.05, respectively (Figure 5c). Additionally, J_{SC} versus I curves shows that the exponent α of 3-BPIC(i), 3-BPIC, and 3-BPIC-F-based devices ($J_{SC} \propto I^\alpha$) are 0.981, 0.984, and 0.986, respectively (Figure S27). The lower n-value and the larger α-value for devices based 3-BPIC-F suggests that the suppressed trap-assisted recombination and reduced bimolecular recombination in 3-BPIC-F-based devices.[47,53] This was further verified by the transient photovoltage (TPV) results (Figure 5d), which showed a longer carrier lifetime (τ) of 63.2 μs for the 3-BPIC-F-based device in comparison with the devices based on 3-BPIC (τ = 57.6 μs) and 3-BPIC(i) (τ = 35.7 μs). To further assess the nonradiative recombination energy loss (ΔE_{nr}), the external electroluminescence yield (EQE_{EL}) was measured against the injection current by operating the OSC device as a light-emitting diode (LED). According to the equation of $\Delta E_{nr} = -k_BT\ln(EQE_{EL})$,[54] the corresponding ΔE_{nr} values are 0.382, 0.245, and 0.237 eV for 3-BPIC(i), 3-BPIC, and 3-BPIC-F-based OSCs, respectively (Figure 5e). The smaller ΔE_{nr} of 3-BPIC-F-based device could be attributed to its uniform dispersion and higher coverage factor on the ITO surface as discussed above. In contrast, the much larger ΔE_{nr} of the 3-BPIC(i)-based device could be attributed to the uneven distribution of 3-BPIC(i) film and the larger interface spacing between ITO and photoactive layer, resulting in a sharp decrease in V_{OC}. Moreover, we performed a Mott−Schottky analysis to investigate the built-in voltage (V_{bi}) of OSCs based on different SAMs. As displayed in Figure 5f, the OSC based on 3-BPIC-F exhibits a V_{bi} of 0.705 V, higher than that of the devices based on 3-BPIC(i) (V_{bi} = 0.542 V) and 3-BPIC (V_{bi} = 0.689 V). The higher V_{bi} of 3-BPIC-F-based device can be

attributed to the lower ΔE_{nr} and larger WF of the ITO/3-BPIC-F substrate, resulting in an enlarged V_{OC}.[55]

3. CONCLUSIONS

In summary, we have successfully developed a novel series of biphosphonic acid molecules with tunable dipole moments for SAMs by modulating the orientation of the phosphonic acid anchoring groups. It is found that, in comparison with the centrosymmetric 3-BPIC(i), the axisymmetric 3-BPIC and 3-BPIC-F exhibit shorter interface spacing, higher E_{ads} with ITO, a larger coverage factor, and better interfacial compatibility. Due to the larger dipole moment and deeper HOMO energy level of 3-BPIC-F, the ITO/3-BPIC-F substrate shows higher WF than that of the ITO/3-BPIC substrate. The advantages of 3-BPIC-F-based SAM not only improve hole selectivity but also reduce interfacial impedance and inhibit nonradiative recombination. As a result, OSCs using SAMs based on axisymmetric 3-BPIC and 3-BPIC-F obtained high PCEs of 19.34% and 19.71%, respectively, along with improved stability. These PCEs are much higher than those achieved from the cells based on centrosymmetric 3-BPIC(i) (PCE = 13.54%). Notably, the large-area (1.0 cm²) device based on 3-BPIC-F delivered an excellent efficiency of 17.25%. Overall, our strategy for regulating the dipole moments of biphosphonic acid molecules provides valuable guidance for designing SAM materials and paves the way for further advancements and commercial applications of OSCs.

■ ASSOCIATED CONTENT

ⓢ Supporting Information

The Supporting Information is available free of charge at https://pubs.acs.org/doi/10.1021/jacs.4c03917.

Materials synthesis, UV−vis, CV, XPS, UPS, KPFM, AFM, AFM-IR, EDS, dark $J-V$, J_{SC}-I measurements, device characterization and stability measurements, DFT theoretical calculations, ^{1}H NMR, ^{13}C NMR, ^{19}F NMR, ^{31}P NMR. and HRMS data (PDF)

■ AUTHOR INFORMATION

Corresponding Authors

Yongsheng Liu − *The Centre of Nanoscale Science and Technology and Key Laboratory of Functional Polymer Materials, Institute of Polymer Chemistry, College of Chemistry and Renewable Energy Conversion and Storage Center, Nankai University, Tianjin 300071, China;* ⓞ orcid.org/0000-0002-7135-723X; Email: liuys@nankai.edu.cn

Yongsheng Chen − *The Centre of Nanoscale Science and Technology and Key Laboratory of Functional Polymer Materials, Institute of Polymer Chemistry, College of Chemistry and Renewable Energy Conversion and Storage Center, Nankai University, Tianjin 300071, China;* ⓞ orcid.org/0000-0003-1448-8177; Email: yschen99@nankai.edu.cn

Authors

Hang Liu − *The Centre of Nanoscale Science and Technology and Key Laboratory of Functional Polymer Materials, Institute of Polymer Chemistry, College of Chemistry, Nankai University, Tianjin 300071, China*

Yufei Xin − *The Centre of Nanoscale Science and Technology and Key Laboratory of Functional Polymer Materials,*

Institute of Polymer Chemistry, College of Chemistry, Nankai University, Tianjin 300071, China

Zhaochen Suo − *The Centre of Nanoscale Science and Technology and Key Laboratory of Functional Polymer Materials, Institute of Polymer Chemistry, College of Chemistry, Nankai University, Tianjin 300071, China*

Liu Yang − *Department of Microelectronic Science and Engineering, Ningbo University, Ningbo 315211, China*

Yu Zou − *The Centre of Nanoscale Science and Technology and Key Laboratory of Functional Polymer Materials, Institute of Polymer Chemistry, College of Chemistry, Nankai University, Tianjin 300071, China*

Xiangjian Cao − *The Centre of Nanoscale Science and Technology and Key Laboratory of Functional Polymer Materials, Institute of Polymer Chemistry, College of Chemistry, Nankai University, Tianjin 300071, China*

Ziyang Hu − *Department of Microelectronic Science and Engineering, Ningbo University, Ningbo 315211, China;*
  orcid.org/0000-0001-7996-2963

Bin Kan − *School of Materials Science and Engineering, National Institute for Advanced Materials, Nankai University, Tianjin 300350, China*

Xiangjian Wan − *The Centre of Nanoscale Science and Technology and Key Laboratory of Functional Polymer Materials, Institute of Polymer Chemistry, College of Chemistry and Renewable Energy Conversion and Storage Center, Nankai University, Tianjin 300071, China;*
  orcid.org/0000-0001-5266-8510

Complete contact information is available at:
https://pubs.acs.org/10.1021/jacs.4c03917

Author Contributions

[1]H.L. and Y.X. contributed equally to this work.

Notes

The authors declare no competing financial interest.

■ REFERENCES

(1) Zhang, G.; Zhao, J.; Chow, P. C. Y.; Jiang, K.; Zhang, J.; Zhu, Z.; Zhang, J.; Huang, F.; Yan, H. Nonfullerene Acceptor Molecules for Bulk Heterojunction Organic Solar Cells. *Chem. Rev.* **2018**, *118* (7), 3447−3507.

(2) Lin, Y.; Adilbekova, B.; Firdaus, Y.; Yengel, E.; Faber, H.; Sajjad, M.; Zheng, X.; Yarali, E.; Seitkhan, A.; Bakr, O. M.; El-Labban, A.; Schwingenschlogl, U.; Tung, V.; McCulloch, I.; Laquai, F.; Anthopoulos, T. D. 17% Efficient Organic Solar Cells Based on Liquid Exfoliated WS$_2$ as a Replacement for PEDOT:PSS. *Adv. Mater.* **2019**, *31* (46), No. 1902965.

(3) Wan, X.; Li, C.; Zhang, M.; Chen, Y. Acceptor−donor−acceptor type molecules for high performance organic photovoltaics - chemistry and mechanism. *Chem. Soc. Rev.* **2020**, *49* (9), 2828−2842.

(4) Li, Y.; Huang, X.; Ding, K.; Sheriff, H. K. M., Jr.; Ye, L.; Liu, H.; Li, C.-Z.; Ade, H.; Forrest, S. R. Non-fullerene acceptor organic photovoltaics with intrinsic operational lifetimes over 30 years. *Nat. Commun.* **2021**, *12* (1), 5419.

(5) Jiang, Y.; Dong, X.; Sun, L.; Liu, T.; Qin, F.; Xie, C.; Jiang, P.; Hu, L.; Lu, X.; Zhou, X.; Meng, W.; Li, N.; Brabec, C. J.; Zhou, Y. An alcohol-dispersed conducting polymer complex for fully printable organic solar cells with improved stability. *Nat. Energy* **2022**, *7* (4), 352−359.

(6) Liu, Y.; Li, B.; Ma, C.-Q.; Huang, F.; Feng, G.; Chen, H.; Hou, J.; Yan, L.; Wei, Q.; Luo, Q.; Bao, Q.; Ma, W.; Liu, W.; Li, W.; Wan, X.; Hu, X.; Han, Y.; Li, Y.; Zhou, Y.; Zou, Y.; Chen, Y.; Li, Y.; Chen, Y.; Tang, Z.; Hu, Z.; Zhang, Z.-G.; Bo, Z. Recent progress in organic solar cells (Part I material science). *Sci. China Chem.* **2022**, *65* (2), 224−268.

(7) Liu, Y.; Liu, B.; Ma, C.-Q.; Huang, F.; Feng, G.; Chen, H.; Hou, J.; Yan, L.; Wei, Q.; Luo, Q.; Bao, Q.; Ma, W.; Liu, W.; Li, W.; Wan, X.; Hu, X.; Han, Y.; Li, Y.; Zhou, Y.; Zou, Y.; Chen, Y.; Liu, Y.; Meng, L.; Li, Y.; Chen, Y.; Tang, Z.; Hu, Z.; Zhang, Z.-G.; Bo, Z. Recent progress in organic solar cells (Part II device engineering). *Sci. China Chem.* **2022**, *65* (8), 1457−1497.

(8) Zhang, G.; Lin, F. R.; Qi, F.; Heumueller, T.; Distler, A.; Egelhaaf, H.-J.; Li, N.; Chow, P. C. Y.; Brabec, C. J.; Jen, A. K. Y.; Yip, H.-L. Renewed Prospects for Organic Photovoltaics. *Chem. Rev.* **2022**, *122* (18), 14180−14274.

(9) Guenther, M.; Kazerouni, N.; Blaette, D.; Perea, J. D.; Thompson, B. C. C.; Ameri, T. Models and mechanisms of ternary organic solar cells. *Nat. Rev. Mater.* **2023**, *8* (7), 456−471.

(10) Lin, Y.; Wang, J.; Zhang, Z.-G.; Bai, H.; Li, Y.; Zhu, D.; Zhan, X. An Electron Acceptor Challenging Fullerenes for Efficient Polymer Solar Cells. *Adv. Mater.* **2015**, *27* (7), 1170−1174.

(11) Zhang, M.; Guo, X.; Ma, W.; Ade, H.; Hou, J. A Large-Bandgap Conjugated Polymer for Versatile Photovoltaic Applications with High Performance. *Adv. Mater.* **2015**, *27* (31), 4655−4660.

(12) Meng, L.; Zhang, Y.; Wan, X.; Li, C.; Zhang, X.; Wang, Y.; Ke, X.; Xiao, Z.; Ding, L.; Xia, R.; Yip, H.-L.; Cao, Y.; Chen, Y. Organic and solution-processed tandem solar cells with 17.3% efficiency. *Science* **2018**, *361* (6407), 1094−1098.

(13) Yuan, J.; Zhang, Y.; Zhou, L.; Zhang, G.; Yip, H.-L.; Lau, T.-K.; Lu, X.; Zhu, C.; Peng, H.; Johnson, P. A.; Leclerc, M.; Cao, Y.; Ulanski, J.; Li, Y.; Zou, Y. Single-Junction Organic Solar Cell with over 15% Efficiency Using Fused-Ring Acceptor with Electron-Deficient Core. *Joule* **2019**, *3* (4), 1140−1151.

(14) Li, C.; Zhou, J.; Song, J.; Xu, J.; Zhang, H.; Zhang, X.; Guo, J.; Zhu, L.; Wei, D.; Han, G.; Min, J.; Zhang, Y.; Xie, Z.; Yi, Y.; Yan, H.; Gao, F.; Liu, F.; Sun, Y. Non-fullerene acceptors with branched side chains and improved molecular packing to exceed 18% efficiency in organic solar cells. *Nat. Energy* **2021**, *6* (6), 605−613.

(15) Zhu, L.; Zhang, M.; Xu, J.; Li, C.; Yan, J.; Zhou, G.; Zhong, W.; Hao, T.; Song, J.; Xue, X.; Zhou, Z.; Zeng, R.; Zhu, H.; Chen, C.-C.; MacKenzie, R. C. I.; Zou, Y.; Nelson, J.; Zhang, Y.; Sun, Y.; Liu, F. Single-junction organic solar cells with over 19% efficiency enabled by a refined double-fibril network morphology. *Nat. Mater.* **2022**, *21* (6), 656−663.

(16) Chen, T.; Li, S.; Li, Y.; Chen, Z.; Wu, H.; Lin, Y.; Gao, Y.; Wang, M.; Ding, G.; Min, J.; Ma, Z.; Zhu, H.; Zuo, L.; Chen, H. Compromising Charge Generation and Recombination of Organic Photovoltaics with Mixed Diluent Strategy for Certified 19.4% Efficiency. *Adv. Mater.* **2023**, *35* (21), No. 2300400.

(17) Hao, S.; Xu, X.; Yu, L.; Peng, S.; Xia, J.; Xie, Y.; Duan, C.; Wu, H.; Li, R.; Peng, Q. Saddle-Shaped Third Component with Out-of-Plane Electrostatic Dipole for Realizing High-Performance Photovoltaic Donor Terpolymers. *Adv. Mater.* **2023**, *35* (29), No. 2301732.

(18) Liang, H.; Bi, X.; Chen, H.; He, T.; Lin, Y.; Zhang, Y.; Ma, K.; Feng, W.; Ma, Z.; Long, G.; Li, C.; Kan, B.; Zhang, H.; Rakitin, O. A.; Wan, X.; Yao, Z.; Chen, Y. A rare case of brominated small molecule acceptors for high-efficiency organic solar cells. *Nat. Commun.* **2023**, *14* (1), 4707.

(19) Pang, B.; Liao, C.; Xu, X.; Yu, L.; Li, R.; Peng, Q. Benzo[d]thiazole Based Wide Bandgap Donor Polymers Enable 19.54% Efficiency Organic Solar Cells Along with Desirable Batch-to-Batch Reproducibility and General Applicability. *Adv. Mater.* **2023**, *35* (21), No. 202300631.

(20) Liu, Q.; Jiang, Y.; Jin, K.; Qin, J.; Xu, J.; Li, W.; Xiong, J.; Liu, J.; Xiao, Z.; Sun, K.; Yang, S.; Zhang, X.; Ding, L. 18% Efficiency organic solar cells. *Sci. Bull.* **2020**, *65* (4), 272−275.

(21) Zhan, L.; Yin, S.; Li, Y.; Li, S.; Chen, T.; Sun, R.; Min, J.; Zhou, G.; Zhu, H.; Chen, Y.; Fang, J.; Ma, C.-Q.; Xia, X.; Lu, X.; Qiu, H.; Fu, W.; Chen, H. Multiphase Morphology with Enhanced Carrier Lifetime via Quaternary Strategy Enables High-Efficiency, Thick-Film, and Large-Area Organic Photovoltaics. *Adv. Mater.* **2022**, *34* (45), No. 202206269.

(22) Zheng, Z.; Hu, Q.; Zhang, S.; Zhang, D.; Wang, J.; Xie, S.; Wang, R.; Qin, Y.; Li, W.; Hong, L.; Liang, N.; Liu, F.; Zhang, Y.; Wei, Z.; Tang, Z.; Russell, T. P.; Hou, J.; Zhou, H. A Highly Efficient Non-Fullerene Organic Solar Cell with a Fill Factor over 0.80 Enabled by a Fine-Tuned Hole-Transporting Layer. *Adv. Mater.* **2018**, *30* (34), No. 1801801.

(23) Sun, W.-J.; Wang, Y.-T.; Zhang, Y.; Sun, B.; Zhang, Z.-Q.; Xiao, M.-J.; Li, X.-Y.; Huo, Y.; Xin, J.; Zhu, Q.; Ma, W.; Zhang, H.-L. A Cathode Interface Layer Based on 4,5,9,10-Pyrene Diimide for Highly Efficient Binary Organic Solar Cells. *Angew. Chem., Int. Ed.* **2022**, *61* (38), No. e202208383.

(24) Zeng, M.; Wang, X.; Ma, R.; Zhu, W.; Li, Y.; Chen, Z.; Zhou, J.; Li, W.; Liu, T.; He, Z.; Yan, H.; Huang, F.; Cao, Y. Dopamine Semiquinone Radical Doped PEDOT:PSS: Enhanced Conductivity, Work Function and Performance in Organic Solar Cells. *Adv. Energy Mater.* **2020**, *10* (25), No. 202000743.

(25) de Jong, M. P.; van Ijzendoorn, L. J.; de Voigt, M. J. A. Stability of the interface between indium-tin-oxide and poly(3,4-ethylenedioxythiophene)/poly(styrenesulfonate) in polymer light-emitting diodes. *Appl. Phys. Lett.* **2000**, *77* (14), 2255−2257.

(26) Wang, Y.; Jiang, W.; Liu, S.-C.; Lin, C.-T.; Fan, B.; Li, Y.; Gao, H.; Liu, M.; Lin, F. R.; Jen, A. K.-Y. Durable Organic Photovoltaics Enabled by a Morphology-Stabilizing Hole-Selective Self-Assembled Monolayer. *Adv. Energy Mater.* **2023**, *14* (5), No. 2303354.

(27) Al-Ashouri, A.; Magomedov, A.; Ross, M.; Jost, M.; Talaikis, M.; Chistiakova, G.; Bertram, T.; Marquez, J. A.; Kohnen, E.; Kasparavicius, E.; Levcenco, S.; Gil-Escrig, L.; Hages, C. J.; Schlatmann, R.; Rech, B.; Malinauskas, T.; Unold, T.; Kaufmann, C. A.; Korte, L.; Niaura, G.; Getautis, V.; Albrecht, S. Conformal monolayer contacts with lossless interfaces for perovskite single junction and monolithic tandem solar cells. *Energy Environ. Sci.* **2019**, *12* (11), 3356−3369.

(28) Jiang, W.; Li, F.; Li, M.; Qi, F.; Lin, F. R. R.; Jen, A. K.-Y. π-Expanded Carbazoles as Hole-Selective Self-Assembled Monolayers for High-Performance Perovskite Solar Cells. *Angew. Chem., Int. Ed.* **2022**, *61* (51), No. e202213560.

(29) Li, Z.; Sun, X.; Zheng, X.; Li, B.; Gao, D.; Zhang, S.; Wu, X.; Li, S.; Gong, J.; Luther, J. M.; Li, Z. a.; Zhu, Z. Stabilized hole-selective layer for high-performance inverted p-i-n perovskite solar cells. *Science* **2023**, *382* (6668), 284−289.

(30) Park, S. M.; Wei, M.; Lempesis, N.; Yu, W.; Hossain, T.; Agosta, L.; Carnevali, V.; Atapattu, H. R.; Serles, P.; Eickemeyer, F. T.; Shin, H.; Vafaie, M.; Choi, D.; Darabi, K.; Jung, E. D.; Yang, Y.; Kim, D. B.; Zakeeruddin, S. M.; Chen, B.; Amassian, A.; Filleter, T.; Kanatzidis, M. G.; Graham, K. R.; Xiao, L.; Rothlisberger, U.; Gratzel, M.; Sargent, E. H. Low-loss contacts on textured substrates for inverted perovskite solar cells. *Nature* **2023**, *624* (7991), 289−294.

(31) Tan, Q.; Li, Z.; Luo, G.; Zhang, X.; Che, B.; Chen, G.; Gao, H.; He, D.; Ma, G.; Wang, J.; Xiu, J.; Yi, H.; Chen, T.; He, Z. Inverted perovskite solar cells using dimethylacridine-based dopants. *Nature* **2023**, *620* (7974), 545−551.

(32) Zhang, S.; Ye, F.; Wang, X.; Chen, R.; Zhang, H.; Zhan, L.; Jiang, X.; Li, Y.; Ji, X.; Liu, S.; Yu, M.; Yu, F.; Zhang, Y.; Wu, R.; Liu, Z.; Ning, Z.; Neher, D.; Han, L.; Lin, Y.; Tian, H.; Chen, W.; Stolterfoht, M.; Zhang, L.; Zhu, W.-H.; Wu, Y. Minimizing buried interfacial defects for efficient inverted perovskite solar cells. *Science* **2023**, *380* (6643), 404−409.

(33) Ullah, A.; Park, K. H.; Lee, Y.; Park, S.; Bin Faheem, A.; Nguyen, H. D.; Siddique, Y.; Lee, K.-K.; Jo, Y.; Han, C.-H.; Ahn, S.; Jeong, I.; Cho, S.; Kim, B.; Park, Y. S.; Hong, S. Versatile Hole Selective Molecules Containing a Series of Heteroatoms as Self-Assembled Monolayers for Efficient p-i-n Perovskite and Organic Solar Cells. *Adv. Funct. Mater.* **2022**, *32* (49), No. 2208793.

(34) Lin, Y.; Firdaus, Y.; Isikgor, F. H.; Nugraha, M. I.; Yengel, E.; Harrison, G. T.; Hallani, R.; El-Labban, A.; Faber, H.; Ma, C.; Zheng, X.; Subbiah, A.; Howells, C. T.; Bakr, O. M.; McCulloch, I.; De Wolf, S.; Tsetseris, L.; Anthopoulos, T. D. Self-Assembled Monolayer Enables Hole Transport Layer-Free Organic Solar Cells with 18% Efficiency and Improved Operational Stability. *ACS Energy Lett.* **2020**, *5* (9), 2935−2944.

(35) Lin, Y.; Zhang, Y.; Zhang, J.; Marcinskas, M.; Malinauskas, T.; Magomedov, A.; Nugraha, M. I.; Kaltsas, D.; Naphade, D. R.; Harrison, G. T.; El-Labban, A.; Barlow, S.; De Wolf, S.; Wang, E.; McCulloch, I.; Tsetseris, L.; Getautis, V.; Marder, S. R.; Anthopoulos, T. D. 18.9% Efficient Organic Solar Cells Based on n-Doped Bulk-Heterojunction and Halogen-Substituted Self-Assembled Monolayers as Hole Extracting Interlayers. *Adv. Energy Mater.* **2022**, *12* (45), No. 2202503.

(36) Truong, M. A.; Funasaki, T.; Ueberricke, L.; Nojo, W.; Murdey, R.; Yamada, T.; Hu, S.; Akatsuka, A.; Sekiguchi, N.; Hira, S.; Xie, L.; Nakamura, T.; Shioya, N.; Kan, D.; Tsuji, Y.; Iikubo, S.; Yoshida, H.; Shimakawa, Y.; Hasegawa, T.; Kanemitsu, Y.; Suzuki, T.; Wakamiya, A. Tripodal Triazatruxene Derivative as a Face-On Oriented Hole-Collecting Monolayer for Efficient and Stable Inverted Perovskite Solar Cells. *J. Am. Chem. Soc.* **2023**, *145* (13), 7528−7539.

(37) Deng, X.; Qi, F.; Li, F.; Wu, S.; Lin, F. R.; Zhang, Z.; Guan, Z.; Yang, Z.; Lee, C.-S.; Jen, A. K.-Y. Co-assembled Monolayers as Hole-Selective Contact for High-Performance Inverted Perovskite Solar Cells with Optimized Recombination Loss and Long-Term Stability. *Angew. Chem., Int. Ed.* **2022**, *61* (30), No. e202203088.

(38) Yip, H.-L.; Hau, S. K.; Baek, N. S.; Ma, H.; Jen, A. K. Y. Polymer solar cells that use self-assembled-monolayer-modified ZnO/Metals as cathodes. *Adv. Mater.* **2008**, *20* (12), 2376−2382.

(39) Kim, S. Y.; Cho, S. J.; Byeon, S. E.; He, X.; Yoon, H. J. Self-Assembled Monolayers as Interface Engineering Nanomaterials in Perovskite Solar Cells. *Adv. Energy Mater.* **2020**, *10* (44), No. 2002606.

(40) Liu, B.; Zhou, Q.; Li, Y.; Chen, Y.; He, D.; Ma, D.; Han, X.; Li, R.; Yang, K.; Yang, Y.; Lu, S.; Ren, X.; Zhang, Z.; Ding, L.; Feng, J.; Yi, J.; Chen, J. Polydentate Ligand Reinforced Chelating to Stabilize Buried Interface toward High-Performance Perovskite Solar Cells. *Angew. Chem., Int. Ed.* **2024**, *63* (8), No. e202317185.

(41) Li, C.; Zhang, Z.; Zhang, H.; Yan, W.; Li, Y.; Liang, L.; Yu, W.; Yu, X.; Wang, Y.; Yang, Y.; Nazeeruddin, M. K.; Gao, P. Fully Aromatic Self-Assembled Hole-Selective Layer toward Efficient Inverted Wide-Bandgap Perovskite Solar Cells with Ultraviolet Resistance. *Angew. Chem., Int. Ed.* **2024**, *63* (1), No. e202315281.

(42) Xin, Y.; Liu, H.; Dong, X.; Xiao, Z.; Wang, R.; Gao, Y.; Zou, Y.; Kan, B.; Wan, X.; Liu, Y.; Chen, Y. Multiarmed Aromatic Ammonium Salts Boost the Efficiency and Stability of Inverted Organic Solar Cells. *J. Am. Chem. Soc.* **2024**, *146* (5), 3363−3372.

(43) Lin, Y.; Magomedov, A.; Firdaus, Y.; Kaltsas, D.; El-Labban, A.; Faber, H.; Naphade, D. R.; Yengel, E.; Zheng, X.; Yarali, E.; Chaturvedi, N.; Loganathan, K.; Gkeka, D.; AlShammari, S. H.; Bakr, O. M.; Laquai, F.; Tsetseris, L.; Getautis, V.; Anthopoulos, T. D. 18.4% Organic Solar Cells Using a High Ionization Energy Self-Assembled Monolayer as Hole-Extraction Interlayer. *ChemSusChem* **2021**, *14* (17), 3569−3578.

(44) Jing, J.; Dong, S.; Zhang, K.; Xie, B.; Zhang, J.; Song, Y.; Huang, F. In-situ self-organized anode interlayer enables organic solar cells with simultaneously simplified processing and greatly improved efficiency to 17.8%. *Nano Energy* **2022**, *93*, No. 106814.

(45) Jing, J.; Dong, S.; Zhang, K.; Zhou, Z.; Xue, Q.; Song, Y.; Du, Z.; Ren, M.; Huang, F. Semitransparent Organic Solar Cells with Efficiency Surpassing 15%. *Adv. Energy Mater.* **2022**, *12* (20), No. 2200453.

(46) Lu, H.; Liu, W.; Ran, G.; Liang, Z.; Li, H.; Wei, N.; Wu, H.; Ma, Z.; Liu, Y.; Zhang, W.; Xu, X.; Bo, Z. High-Pressure Fabrication of Binary Organic Solar Cells with High Molecular Weight D18 Yields Record 19.65 % Efficiency. *Angew. Chem., Int. Ed.* **2023**, *62* (50), No. e202314420.

(47) Yu, X.; Ding, P.; Yang, D.; Yan, P.; Wang, H.; Yang, S.; Wu, J.; Wang, Z.; Sun, H.; Chen, Z.; Xie, L.; Ge, Z. Self-Assembled Molecules with Asymmetric Backbone for Highly Stable Binary Organic Solar Cells with 19.7 % Efficiency. *Angew. Chem., Int. Ed.* **2024**, *136*, No. e202401518.

(48) Blom, P. W. M.; Mihailetchi, V. D.; Koster, L. J. A.; Markov, D. E. Device Physics of Polymer:Fullerene Bulk Heterojunction Solar Cells. *Adv. Mater.* **2007**, *19* (12), 1551−1566.

(49) Ma, Y.; Zhang, M.; Wan, S.; Yin, P.; Wang, P.; Cai, D.; Liu, F.; Zheng, Q. Efficient Organic Solar Cells from Molecular Orientation Control of M-Series Acceptors. *Joule* **2021**, *5* (1), 197−209.

(50) Yao, J.; Ding, S.; Zhang, R.; Bai, Y.; Zhou, Q.; Meng, L.; Solano, E.; Steele, J. A.; Roeffaers, M. B. J.; Gao, F.; Zhang, Z.-G.; Li, Y. Fluorinated Perylene-Diimides: Cathode Interlayers Facilitating Carrier Collection for High-Performance Organic Solar Cells. *Adv. Mater.* **2022**, *34* (32), No. 2203690.

(51) Afroz, M. A.; Aranda, C. A.; Tailor, N. K.; Yukta; Yadav, P.; Tavakoli, M. M.; Saliba, M.; Satapathi, S. Impedance Spectroscopy for Metal Halide Perovskite Single Crystals: Recent Advances, Challenges, and Solutions. *ACS Energy Lett.* **2021**, *6* (9), 3275−3286.

(52) Proctor, C. M.; Kuik, M.; Thuc-Quyen, N. Charge carrier recombination in organic solar cells. *Prog. Polym. Sci.* **2013**, *38* (12), 1941−1960.

(53) Liu, D.; Kan, B.; Ke, X.; Zheng, N.; Xie, Z.; Lu, D.; Liu, Y. Extended Conjugation Length of Nonfullerene Acceptors with Improved Planarity via Noncovalent Interactions for High-Performance Organic Solar Cells. *Adv. Energy Mater.* **2018**, *8* (26), No. 1801618.

(54) Vandewal, K.; Benduhn, J.; Nikolis, V. C. How to determine optical gaps and voltage losses in organic photovoltaic materials. *Sustain. Energy Fuels* **2018**, *2* (3), 538−544.

(55) Wetzelaer, G.-J. A. H.; Blom, P. W. M. Diffusion-driven currents in organic-semiconductor diodes. *Npg Asia Mater.* **2014**, *6* (7), No. e110.